

A new method to estimate local pitch angles in spiral galaxies: Application to spiral arms and feathers in M81 and M51

Ivânio Puerari¹, Bruce G. Elmegreen², David L. Block³

ABSTRACT

We examine $8\mu\text{m}$ IRAC images of the grand design two-arm spiral galaxies M81 and M51 using a new method whereby pitch angles are locally determined as a function of scale and position, in contrast to traditional Fourier transform spectral analyses which fit to average pitch angles for whole galaxies. The new analysis is based on a correlation between pieces of a galaxy in circular windows of $(\ln R, \theta)$ space and logarithmic spirals with various pitch angles. The diameter of the windows is varied to study different scales. The result is a best-fit pitch angle to the spiral structure as a function of position and scale, or a distribution function of pitch angles as a function of scale for a given galactic region or area. We apply the method to determine the distribution of pitch angles in the arm and interarm regions of these two galaxies. In the arms, the method reproduces the known pitch angles for the main spirals on a large scale, but also shows higher pitch angles on smaller scales resulting from dust feathers. For the interarms, there is a broad distribution of pitch angles representing the continuation and evolution of the spiral arm feathers as the flow moves into the interarm regions. Our method shows a multiplicity of spiral structures on different scales, as expected from gas flow processes in a gravitating, turbulent and shearing interstellar medium. We also present results for M81 using classical 1D and 2D Fourier transforms, together with a new correlation method, which shows good agreement with conventional 2D Fourier transforms.

Subject headings: galaxies: fundamental parameters – galaxies: individual (M81, M51) – galaxies: spiral – galaxies: structure – methods: numerical

¹Instituto Nacional de Astrofísica, Óptica y Electrónica, Calle Luis Enrique Erro 1, 72840 Santa María Tonantzintla, Puebla, Mexico (puerari@inaoep.mx)

²IBM T. J. Watson Research Center, 1101 Kitchawan Road, Yorktown Heights, New York 10598 USA

³School of Computational and Applied Mathematics, University of Witwatersrand, Private Bag 3, WITS 2050, South Africa

1. Introduction

Disk galaxies support stellar spiral density waves (Bertin et al. 1989) that interact with each other at resonances (Tagger et al. 1987) to produce complex, regenerating structures (see review in Sellwood 2014). These waves also interact with the gas to produce even more complex structures, including gas clumps in the arms (Kim & Ostriker 2001), gas feathers downstream from the main arms (Kim & Ostriker 2002), and multiple shocks (Lugovskii & Filistov 2014). These and other gas structures have further connections with star formation, which can produce its own structure, such as shells, pillars, and local blowout cavities (see review in Elmegreen 2012). The quantification of all this structure for the purpose of comparing different regions or different galaxies, or comparing theory with observations, is difficult because the structure is multi-scale, multi-component (gas, old stars, young stars, etc.), and spatially varying.

Here we describe a new method for quantifying spiral structure and its spatial variations covering a wide range of scales. We apply this method to the characterization of spiral arms and feathers for two grand design galaxies, M81 and M51. The $8\mu\text{m}$ images from Spitzer are used because they show essentially all of the diffuse gas structures in PAH emission with high angular resolution; $0.748''$ for M81, which is 13 pc for a distance of 3.6 Mpc, and $1.222''$ for M51, which is 63 pc for a distance of 10.6 Mpc (NASA/IPAC Extragalactic Database, <http://ned.ipac.caltech.edu>).

Sandage (1961) noted the prominence of dust lanes in late-type spiral galaxies, describing stellar “branches” in the main arms and dust “filaments” that cut across the arms, especially in the case of M51. Lynds (1970) studied 17 late-type spirals using archival photographic plates from the Mount Wilson and Palomar observatories. She also noted the presence of main dust lanes in the arms and thin “feathers” of dust with large pitch angles cutting across the arms. Weaver (1970) placed the sun in a stellar “spur” or “offshoot” of the Sagittarius arm in the Milky Way. Elmegreen (1980) studied seven spirals to investigate in more detail the properties of *stellar* spurs and determined that they have pitch angles $\sim 50^\circ$ larger than the main arms. She noted that gaseous feathers and stellar spurs have similar pitch angles and suggested they may have a common origin (see also Piddington 1973). A large survey of dust feathers in spiral galaxies was conducted by La Vigne (2006) using archival data from the Hubble Space Telescope. They found a decrease in spur separation with increasing gas density, suggesting that gravitational instabilities are involved. Periodic dust feathers occurred in 20% of their Sb and Sc types.

In what follows, we define “spurs” as interarm stellar features that jut out from otherwise continuous stellar arms, as distinct from branches, where one arm ends and turns into two arms further out. Similarly, we define “feathers” as gas or dust features that jut out from

the main stellar arms. These terms are consistent with the usages referenced above. The present study is about feathers because we use dust emission to delineate the structures.

Interarm dust feathers were first seen in emission at $15\mu\text{m}$ for M51 (Block et al. 1997) with ISOCAM (Cesarsky et al. 1996). They were first seen at arcsec resolution in M81 with Spitzer $8\mu\text{m}$ images (Willner et al. 2004). Feathers are bright in molecular line emission as well, and they often have associated $\text{H}\alpha$ (for M51, see Scoville et al. 2001; Corder et al. 2008; Koda et al. 2009; Schinnerer et al. 2013). Chandar et al. (2011) note that two prominent feathers in M51 contain clusters $\sim 10^8$ yrs old and suggest this is consistent with simulations of global spiral density wave arms in Dobbs & Pringle (2010).

Efforts to explain spurs and feathers began with Balbus (1988), who performed a local gas dynamical stability analysis of a single-fluid polytropic flow through a spiral arm. He found that gravitational instabilities in the presence of reverse shear and expansion downstream from the arm can be reinforced by epicyclic motions and lead to the growth of features with large pitch angles. Two-dimensional, time-dependant, magnetohydrodynamic simulations of a self-gravitating, differentially rotating piece of a gas disk with a steady spiral potential were studied by Kim & Ostriker (2002). They also found that gravitational instabilities in the compressed arm gas produced feathers downstream as a result of expansion and reverse shear. Extension to three-dimensions confirmed these results, although the separation between feathers increased because of the dilution of the in-plane component of gravity (Kim & Ostriker 2006). Chakrabarti et al. (2003) studied the growth of small-scale gas features in a steadily imposed stellar spiral wave, finding feathers, branches, and other chaotic features with a link to ultraharmonic resonances and gravitational instabilities in the arms.

Wada & Koda (2004) discovered an additional “wobble” instability that operates even without self-gravity when the reverse shear downstream from an arm triggers something like a Kelvin-Helmholtz instability. Magnetic fields (Shetty & Ostriker 2006; Dobbs & Price 2008) and three-dimensional effects such as vertical shear (Kim & Ostriker 2006) may stabilize this, however. Dwarkadas & Balbus (1996) suggested that the radial component of the post-shock flow stabilizes the Kelvin-Helmholtz instability. Kim et al. (2014) looked at the wobble instability again and showed analytically and with hydrodynamic non-gravitating simulations that it can arise from accumulated potential vorticity in gas that flows successively through many irregular shock fronts. They also explained why Dwarkadas & Balbus (1996) did not see the instability; i.e., the growth rate for their long wavelength perturbations was too slow. Dobbs & Bonnell (2006) also got interarm feathers without self-gravity, from sheared and expanded gas structures that form randomly in the cold gas of spiral arms and then flow into the interarm region.

Shetty & Ostriker (2006) extended the Kim & Ostriker (2002) two-dimensional self-gravitating simulations to global scales and confirmed that feathers grow from perturbations in spiral shocks for the inner regions. In the outer regions, they found that interarm filaments can grow by local self-gravity even without an imposed spiral. Wada (2008) included realistic heating and cooling in a three-dimensional self-gravitating hydrodynamics simulation with an imposed spiral and found feathers connected with the main shocks. In contrast, Wada et al. (2011) got no spurs or feathers in N-body+SPH models with live stars and gas because the spirals corotated with the disk while forming and re-forming, and the gas fell into the spiral potential from both sides. In all of these models, gas irregularities in the flow through a spiral wave of stars is required for feather formation downstream.

Recently, Lee & Shu (2012) and Lee (2013) present an analytic formulation of two-dimensional feathering in a magnetic, self-gravitating gas that circulates in a galaxy with a steady stellar spiral. This formulation involves perturbing the shocked flow in spiral coordinates. A similar procedure was followed by Elmegreen (1991) to determine the growth rate and effective Toomre Q for shearing gravitational instabilities in a regular spiral density wave flow. Both studies suggest that these instabilities drive the formation of giant molecular clouds and star formation in spiral galaxies (see also Khoperskov et al. 2013; Elmegreen et al. 2014).

Kim & Kim (2014) studied angular momentum transfer and radial gas drift in two-dimensional hydrodynamical simulations of gas flow in an imposed spiral arm potential. They show the density distribution in the $(\ln R, \theta)$ plane, which is similar to our display here. Interarm feathers with large pitch angles are clearly present in their work, and they are connected with density irregularities in the spiral arm shocks.

Renaud et al. (2013) performed an N-body/adaptive mesh simulation of a Milky Way-size galaxy at extremely high resolution and got curled spiral arm structures that resembled Kelvin-Helmholtz instabilities. They made a distinction between small-scale structures, which host star formation at their tips, and extended lower-density interarm structures, which have no star formation.

To provide a quantitative basis for these studies, we introduce a method to determine the distribution of pitch angles for spiral arms and their smaller scale substructures. Using M81 and M51 as examples (Section 2), we first review the standard Fourier transform techniques and introduce an improved method using correlations in 2π azimuthal windows, which give results in agreement with the Fourier techniques (Section 3). Section 4 then presents a better method that calculates correlations using small circular windows in $(\ln R, \theta)$ space. This gives local pitch angles at different scales, depending on the window size. Finally, in Section 5, we present the results of this new method for M81 and M51.

2. The data

Incorporating large-format infrared detector arrays, with the intrinsic sensitivity of a cryogenically-cooled mirror and the high observing efficiency of a heliocentric orbit, the Spitzer Space Telescope gives unparalleled opportunities to study spiral galaxy morphology and dust grain emission. The IRAC instrument (Fazio et al. 2004) comprises four detectors, which after launch in August 2003, operated for several years at four wavelengths, these being $3.6\ \mu\text{m}$ (channel 1), $4.5\ \mu\text{m}$ (channel 2), $5.8\ \mu\text{m}$ (channel 3) and $8.0\ \mu\text{m}$ (channel 4). The IRAC filter band center is $7.87\ \mu\text{m}$ in channel 4 (see Gehra et al. 2007).

For both M81 and M51, we selected IRAC channel 4, wherein one observes emission from ultra-small ($\sim 0.01\mu\text{m}$) dust grains as well as from macromolecules (the 8 micron band contains emission from polycyclic aromatic hydrocarbons (PAHs) at $\lambda = 7.7$ microns). Small carbonaceous grains and PAHs undergo temperature spiking (Greenberg 1968; Sellgren 1984; Greenberg & Li 1996; Li 2004) and can become hotter than 1000K - 2000K as they transiently absorb a photon from the interstellar radiation field. It is primarily the emission from such warm (~ 60 K) tiny dust grains and PAHs, subject to temperature spiking, which is detected at 8 microns. As emphasized by Bendo et al. (2008), PAH $8\mu\text{m}$ emission seems to appear in shell-like features around star-forming regions, and is thus an excellent tracer of these. In contrast, longer wavelength $24\mu\text{m}$ emission is shown by Bendo et al. (2008) to peak within star-forming regions. Channel 4 is thus our preferred choice to trace spiral arm structure, as well as star formation, in the disks of M81 and M51. Our re-binned channel 4 images of M81 and M51 have scales of $0.748''\ \text{pixel}^{-1}$ and $1.222''\ \text{pixel}^{-1}$, respectively.

3. 1D and 2D Fourier techniques & a correlation method

The most common way to quantify m -armed spiral structure in disk galaxies is with 1D Fourier transforms of the azimuthal profiles (see e.g. Grosbøl 2004). Essentially, for each azimuthal profile $I_R(\theta)$, the order- m Fourier coefficients A_m are calculated as functions of radius R using the equation

$$A_m(R) = \int_{-\pi}^{\pi} I_R(\theta) e^{-im\theta} d\theta. \quad (1)$$

The amplitude of $A_m(R)$ determines the radial region where a given m structure is important; the phase of $A_m(R)$ can be used to estimate the pitch angle of the order- m spiral arm.

Bidimensional Fourier techniques have been discussed in a number of papers (e.g., Kalnajs 1975; Considère & Athanassoula 1982; Iye et al. 1982; Krakow 1982; Puerari & Dottori 1992; Puerari 1993; Block & Puerari 1999; Puerari et al. 2000, amongst others). They give

global pitch angles, averaged over a galaxy, or average pitch angles as a function of galactocentric radius (Savchenko 2012; Davis et al. 2012). The bidimensional Fourier coefficients $A(m, p)$ in a basis of logarithmic spirals can be calculated as

$$A(m, p) = \int_{u_{min}}^{u_{max}} \int_{-\pi}^{\pi} I(u, \theta) e^{-i(m\theta + pu)} d\theta du \quad (2)$$

where $u = \ln R$, m is the azimuthal frequency (related to θ), and p is the frequency related to $\ln R$. The pitch angle P of the order- m spiral arm is given by $\tan P = -m/p$. $I(u, \theta)$ is the light distribution of the galaxy in a (u, θ) plane. Hence, once the radial annulus to be analyzed is chosen by fixing u_{min} and u_{max} , the amplitude of the complex matrix $A(m, p)$ will show the most probable pitch angle P of that m structure in the annulus.

We discuss now a new method to extract the same information as the bidimensional Fourier transform. We construct a family of synthetic logarithmic spirals inside a 2π window in $(\ln R, \theta)$ coordinates, i.e., with a given $\Delta \ln R$ and $\Delta \theta = 2\pi$ for radius R and azimuthal angle θ . The synthetic spirals have a pitch angle P and a number of arms m , so their curves of constant phase are given by $\ln R = \frac{m}{p}\theta + \Phi$ for some constant Φ . The pitch angle P of the spiral in this formalism is given by $\tan P = \frac{\Delta R}{R\Delta\theta} = \frac{\Delta \ln R}{\Delta\theta} = -\frac{m}{p}$.

The phase of the spiral is defined to be zero, which corresponds to the crest of the synthetic arm, at the center of the window, so that $\Phi = \ln R_{min} + 0.5\Delta \ln R$ for minimum window radius R_{min} . Then the synthetic spiral, S , is the cosine function of the phase,

$$S_{m,p}(\ln R, \theta) = \cos(m\theta + p \ln R + p \ln R_{mid}) \quad (3)$$

With this definition of Φ , the synthetic arm peak is in the middle of the window for all assumed m and p . Note that for $p > 0$, the azimuthal angle increases in the usual sense for cylindrical coordinates, counter-clockwise, as the radius increases, corresponding to a “Z”-type morphology, while for $p < 0$, the spiral has an “S”-type morphology.

The deprojected image I of a galaxy - now sampled in a $(\ln R, \theta)$ plane - is then cross-correlated with the synthetic logarithmic spiral, giving the correlation

$$C_m(\ln R, \theta, p) = \sum_x \sum_y S_{m,p}(\ln R + y, \theta + x) I(\ln R, \theta) \quad (4)$$

where the summation is over pixels in the range $x = -\pi$ to π and $y = \ln R - 0.5\Delta \ln R$ to $\ln R + 0.5\Delta \ln R$. This is the sum over the local (x, y) coordinates inside the window. There is a different correlation sum for each image coordinate $(\ln R, \theta)$, and for each p and m , i.e., C is a 4 dimensional matrix. The pitch angle for an m structure at a given radius $\ln R_{mid}$, is calculated using the p of the the maximum $C_m(\ln R_{mid}, \theta, p)$, maximized in θ .

This corresponds to the best-fit pitch angle for an m -arm spiral going through the image coordinate $(\ln R_{mid}, \theta)$.

The results of the application of the techniques discussed above are shown for M81 in Figures 1 to 4. In Figure 1, we display the deprojected $8\mu\text{m}$ image of M81 ($PA = 157^\circ$ and inclination $\omega = 58^\circ$, de Vaucouleurs et al. 1991) in 2 ways: in the plane of the galaxy, and in $(\ln R, \theta)$ space. Figure 2 displays the results of the application of equation 1. The amplitudes of the m coefficients show that $m = 2$ is the most prominent feature for this grand design galaxy. We can distinguish two “sets” of $m = 2$ structures: one from $R = 150$ to $R = 247$ arcsec and another from $R = 247$ to $R = 606$ arcsec. Figure 3 shows results for the 2D Fourier transform as a function of radius (Savchenko 2012) and for our correlation method (2π window) for $\Delta \ln R = u_{max} - u_{min} = 0.35$. Note that our correlation method using m synthetic spirals in a 2π window give results very similar to those coming from a 2D Fourier transform. Finally, in Figure 4 we plot the estimation of pitch angles for the $m = 2$ component as a function of radius for three different techniques: Savchenko (2012), Davis et al. (2012) and our correlation method (2π window). Note that Savchenko’s and our methods agree very well for all radii. Davis et al. (2012) only changed $\ln R_{min}$ in their 2D Fourier transform. Definitely, the inner point calculated with the Davis et al. method is affected by the outer structures.

4. A new correlation method: circular windows in the $(\ln R, \theta)$ space

Having checked our correlation method in a 2π window and getting results in full agreement to those coming from the 2D Fourier transform, we introduce a new method, now using circular windows in $(\ln R, \theta)$ space. By using these new windows, we no longer have a restriction on m symmetry. Furthermore, by changing the diameter of the window, we can study the distribution of the pitch angles at various scales. Inside each window, we define a filter which is a sine function from 0 to π , i.e., we have the maximum of the filter at its center, and the values falling to zero at the borders of the window (Figure 5). So, for each galaxy image, and for each position in $(\ln R, \theta)$ space, we correlate the galaxy image with the filter function for different pitch angles and window diameters. Let’s describe the filter as $F = F(\ln R_c, \theta_c, P_w, D_w)$, that is the circular filter centered at $(\ln R_c, \theta_c)$, with pitch angle P_w , in a window of diameter D_w . We have analysed our images for pitch angles P_w from -1° to -90° and from $+90^\circ$ to $+1^\circ$, and for four different D_w with values 0.1, 0.2, 0.35 and 0.51 in units of $\ln R$. The algorithm first transforms the deprojected (x, y) image of a galaxy to

a $(\ln R, \theta)$ matrix. Our correlation method can be described as

$$C(\ln R_c, \theta_c, P_w, D_w) = \frac{\sum_{i=1,N} F(\ln R_c, \theta_c, P_w, D_w) I(\ln R, \theta)}{\sum_{i=1,N} I(\ln R, \theta)} \quad (5)$$

where $\sum_{i=1,N}$ represents the summation over the $N = \pi(D_w/2)^2$ pixels on the circular window. $\sum_{i=1,N} I(\ln R, \theta)$ is a normalization factor. The correlation will be higher when the pitch angle of some structure centered at $(\ln R_c, \theta_c)$ coincides with the pitch angle of the filter F . By changing the diameter of the window, different spatial scales can be analyzed.

5. Results for the locally determined pitch angles at different scales

We deprojected the Spitzer $8\mu\text{m}$ image of M81 using the values of $PA = 157^\circ$ and inclination $\omega = 58^\circ$ (de Vaucouleurs et al. 1991). For M51, $PA = 170^\circ$ and inclination $\omega = 20^\circ$ were taken, following Shetty et al. (2007). The deprojected images were subjected to our cross correlation method, using sine filters on circular windows in the $(\ln R, \theta)$ space as described above.

In Figure 6 we present once again M81 in (x, y) and $(\ln R, \theta)$, but now we delineate the areas in which we add all the correlations calculated for a given window diameter for each pitch angle. Four areas were chosen, two over the arms (blue and red), and two placed in the interarm regions (green and black). The minimum and maximum radii for the regions are 330 and 525 arcsec, or $\ln R = 5.8$ and 6.26. As already noted, we use four different window diameters $D_w = 0.1, 0.2, 0.35$, and 0.51 in units of $\ln R$. These circular windows are drawn in the bottom panel of the figure, and represent the sizes of the features we are measuring.

Figure 7 shows the sum of correlations in each area for the different window diameters, as a function of pitch angle (left panels, interarm regions; right panels, arm regions). Thicker lines represent larger window diameters and therefore represent longer spiral structures. Thinner lines represent the smaller scale structures related to feathers. For the interarm regions (green and black) and at smaller scales, we have a broad range of pitch angles. For the black area, the distribution of pitch angles has a peak at $P = -28^\circ$. For larger scales, the distribution is affected by the main spiral arms at the azimuthal edge of the analysed areas; pitch angles $P = 90^\circ - P_{\text{spiral}}$ therefore get larger correlations (P_{spiral} is the pitch angle of the main spiral structure).

For the arm regions in Figure 7 (blue and red), the small scales present a broad distribution of pitch angles and the large scales show the main $m = 2$ structure of this galaxy, which has a pitch angle of $P \sim -17^\circ$ (see the marked peak for the red region in Figure 7; see also Section 3). The arm inside the blue area has two main components with $P \sim -22^\circ$

and $P \sim -10^\circ$. These two peaks can be recognized in the blue area in Figure 6, bottom panel. At smaller radii, there is a bright structure presenting a more open pitch angle. The structure at large radius is similar to that in the red area.

In Figure 8, we present a zoom of the sum of correlations for one interarm (black) and one arm (red) region, for the two intermediate scales $D_w = 0.2$ and 0.35 . The arm peaks at a pitch angle around $P = -17^\circ$, but for the interarm region, the sum of the correlations points to a more open structure, with a broader distribution in pitch angles and a peak around $P = -28^\circ$.

As discussed in the introduction, observations by La Vigne (2006) and others show that feathers are more open compared to main spiral arms (see their Figures 1 and 2 where they outline the feathers they detect by eye in M51 and NGC 628). Numerical simulations (e.g., Kim & Kim 2014) also show that sub-structures evolving from the main arms into the interarm regions have larger pitch angles compared to the main spiral.

In Figure 9, we show a sketch of the results of Figure 8. The main spiral arm in the red region has $P = -17^\circ$ and is designated by a thick red curve. The dashed lines in the black region have $P = -28^\circ$. These calculated values agree well with the structures in the figure.

Figures 10 to 12 are similar to Figures 6 to 8, but now for M51. The observed $(\ln R, \theta)$ map resembles the model at slow pattern speed in Kim & Kim (2014). Figure 10 delineates the areas we analysed for M51. We use minimum and maximum radii of 44 and 106 arcsec, or $\ln R = 3.78$ and 4.66 . Figure 11 shows the sum of the correlations for all regions. As for M81, the interarm regions on small scales present a broad distribution of pitch angles up to a large value (see the arrows in the left panels). The interarms on large scales have a pitch angle distribution that is dominated by the main spiral arms, giving large correlations for $P = 90^\circ - P_{\text{spiral}}$. For the arm regions (right panels), the spiral arm in the red region is more symmetric than the arm in the blue region. The main peak for the spiral arm in the blue region is quite asymmetric. Here again we find secondary peaks for pitch angles larger than the pitch angle of the main spiral arms. In Figure 12 the pitch angle for the main spiral arm in the red region is $P = -19^\circ$, with a secondary bump for $P \sim -52^\circ$ (bottom panel). The structures in the interarm region have larger pitch angles, $P \leq -40^\circ$.

The pitch angles determined for the $m = 2$ spiral arms are $P \sim -18^\circ$ for M81 and $P \sim -19^\circ$ for M51. For M81, Lendall et al. (2008) used Spitzer IRAC 3.6 and $4.5\mu\text{m}$ images to make an “eye-ball” fit giving $P \sim -23^\circ$. Bash & Kaufman (1986) estimated the pitch angles in radio continuum maps. They noticed that the two main arms differ in pitch angles, deriving $P \sim -17^\circ$ for the eastern arm and $P \sim -23^\circ$ for the western arm. Similar numbers were determined with bidimensional Fourier transforms by Puerari et al. (2009) in

a multiwavelength study using GALEX and Spitzer IRAC images. For M51, Shetty et al. (2007) used the CO distribution to determine a pitch angle of $P = -21.1^\circ$. More recently, Hu et al. (2013) used $P = -17.5^\circ$ from their models of M51. Fletcher et al. (2011) report an average pitch angle of $P = -20^\circ$. Evidently, many methods give similar results for the pitch angles of the main spiral arms in these two galaxies. Here we reproduce those values on large scales, but also find a broad range of values up to larger pitch angles on small scales. There is a multiplicity of spiral structures on different scales, as expected from gas flows in gravitating, turbulent and shearing interstellar media.

I.P. acknowledges support from the Mexican foundation CONACyT and from the University of the Witwatersrand.

REFERENCES

- Balbus, S. A. 1988, ApJ, 324, 60
- Bash, F. N. & Kaufman, M. 1986, ApJ, 310, 621
- Bendo, G.J., Draine, B.T., Engelbracht, C.W. et al. 2008, MNRAS, 389, 629
- Bertin, G., Lin, C.C., Lowe, S.A., & Thurstans, R.P., 1989, ApJ, 338, 78
- Block, D., Elmegreen, B. G., Stockton, A., & Sauvage, M. 1997, ApJL, 486, 95.
- Block, D.L. & Puerari, I., 1999, A&A, 342, 627
- Chakrabarti, S., Laughlin, G., & Shu, F. H. 2003, ApJ, 596, 220
- Chandar, R., Whitmore, B. C., Calzetti, D., et al. 2011, ApJ, 727, 88
- Cesarsky, C. J., et al. 1996, A&A, 315, L32
- Considère, S. & Athanassoula, E. 1982, A&A, 111, 28
- Corder, S., Sheth, K., Scoville, N. Z., Koda, J., Vogel, S. N., & Ostriker, E. C. 2008, ApJ, 689, 148
- Davis, B. L., Berrier, J. C., Shields, D. W., Kennefick, J., Kennefick, D., Seigar, M. S., Lacy, C. H. S., & Puerari, I. 2012, ApJS, 199, 33
- de Vaucouleurs, G., de Vaucouleurs, A., Corwin, H.G., Buta, R.J., Paturel, G., & Fouqué, P. 1991, Third Reference Catalogue of Bright Galaxies (Springer Verlag New York)

- Dobbs, C L., & Bonnell, I. A. 2006, MNRAS, 367, 873
- Dobbs, C. L., & Price, D. J. 2008, MNRAS, 383, 497
- Dobbs, C. L., & Pringle, J. E. 2010, MNRAS, 409, 396
- Dwarkadas, V.V, & Balbus, S.A. 1996, ApJ, 467, 87
- Elmegreen, D. M. 1980, ApJ, 242, 528
- Elmegreen, B. G. 1991, ApJ, 378, 139
- Elmegreen, B. G. 2012, IAUS 284, eds. R.J. Tuffs & C.C. Popescu, Cambridge: Cambridge University, p. 317
- Elmegreen, D. M., Elmegreen, B. G., Erroz-Ferrer, S., et al. 2014, ApJ, 780, 32
- Fazio, G.G., Hora, J.L., Allen, L.E., et al. 2004, ApJS, 154, 10
- Fletcher, A., Beck, R., Shukurov, A., Berkhuijsen, E. M., & Horellou, C. 2011, MNRAS, 412, 2396
- Gehrz, R.D., et al. 2007, Rev. Sci. Instrum. 78, 011302
- Greenberg, J.M., 1968, in Stars and Stellar Systems, vol VII, eds. Middlehurst, B.M. and Aller, L.H., University of Chicago Press, 221
- Greenberg, J.M., & Li, A. 1996, in New Extragalactic Perspectives in the New South Africa, eds. Block, D.L. and Greenberg, J.M. 118
- Grosbøl, P., Patsis, P. A., & Pompei, E. 2004, A&A, 423, 849
- Hu, T., Shao, Z, & Peng, Q. 2013, ApJL, 762, 1
- Iye, M., Okamura, S., Hamabe, M., & Watanabe, M., 1982, ApJ, 256, 103
- Kalnajs, A.J., 1975, in La Dynamique des Galaxies Spirales, ed. L. Weliachew (Paris Editions du CNRS), 103
- Kendall, S., Kennicutt, R. C., Clarke, C., & Thornley, M. D. 2008, MNRAS, 387, 1007
- Khoperskov, S. A., Vasiliev, E. O., Sobolev, A. M., & Khoperskov, A. V. 2013, MNRAS, 428, 2311
- Kim, Y., & Kim, W.-T. 2014, MNRAS, 440, 208

- Kim, W.-T., & Ostriker, E.C. 2001, *ApJ*, 559, 70
- Kim, W.-T., & Ostriker, E. C. 2002, *ApJ*, 570, 132
- Kim, T.-T., & Ostriker, E.C. 2006, *ApJ*, 646, 213
- Kim, W.-T., Kim, Y., & Kim, J.-G. 2014, arXiv1405.5874
- Koda, J., Scoville, N., Sawada, T., et al. 2009, *ApJ*, 700, L132
- Krakow, W., Huntley, J. M., & Seiden, P. E. 1982, *AJ*, 87, 203
- La Vigne, M. A., Vogel, S. N., & Ostriker, E. C. 2006, *ApJ*, 650, 818
- Lee, W.-K. 2013, PhD Thesis, University of California, San Diego
- Lee, W.-K., & Shu, F. H. 2012, *ApJ* 756, 45
- Li, A., 2004, in *Penetrating bars through masks of cosmic dust: the Hubble tuning fork strikes a new note*, eds. D.L. Block, I. Puerari, K.C. Freeman, R. Groess, and E.K. Block, Kluwer, Dordrecht, 535
- Lynds, B.T. 1970, in *IAU Symp. 38, The Spiral Structure of our Galaxy*, eds. W. Becker and G. I. Contopoulos, Dordrecht, Reidel, 26
- Lugovskii, A. Yu., & Filistov, E. A. 2014, *Astronomy Reports*, 58, 48
- Piddington, J. H. 1973, *ApJ*, 179, 755
- Puerari, I., Block, D.L., Elmegreen, B. G., Frogel, J.A., & Eskridge, P.B., 2000, *A&A*, 359, 932
- Puerari, I., & Dottori H.A. 1992, *A&AS*, 93, 469
- Puerari, I., González-Lópezlira, R. A., & Valdez-Gutiérrez, M. 2009, in *New Quests in Stellar Astrophysics. II. Ultraviolet Properties of Evolved Stellar Populations*, eds. M. Chavez, E. Bertone, D. Rosa-Gonzalez, and L. H. Rodriguez-Merino, Springer, 99
- Puerari, I. 1993, *PASP*, 105, 1290
- Renaud, F., Bournaud, F., Emsellen, E., et al. 2013, *MNRAS* 436, 1836
- Sandage, A. 1961, *The Hubble Atlas of Galaxies*
- Savchenko, S. S. 2012, *Astrophysical Bulletin*, 67, 310

- Schinnerer, E., Meidt, S. E., Pety, J., et al. 2013, *ApJ*, 779, 42
- Scoville, N. Z., Polletta, M., Ewald, S., Stolovy, S. R., Thompson, R., & Rieke, M. 2001, *AJ*, 122, 3017
- Sellgren, K. 1984, *ApJ*, 277, 623
- Sellwood, J. 2014. *Reviews of Modern Physics*, 86, 1
- Shetty, R., Vogel, S. N., Ostriker, E. C., & Teuben, P. J. 2007, *ApJ*, 665, 1138
- Shetty, R., & Ostriker, E.C. 2006, *ApJ*, 647, 997
- Tagger, M., Sygnet, J. F., Athanassoula, E., & Pellat, R. 1987, *ApJ*, 318, L43
- Wada, K., & Koda J. 2004, *MNRAS*, 349, 270
- Wada, K. 2008, *ApJ*, 675, 188
- Wada, K., Baba, J., & Saitoh, T.R. 2011, *ApJ*, 735, 1
- Weaver, H. 1970, *IAUS*, 38, 126
- Willner, S. P., Ashby, M. L. N., Barmby, P., et al. 2004 *ApJS*, 154, 222

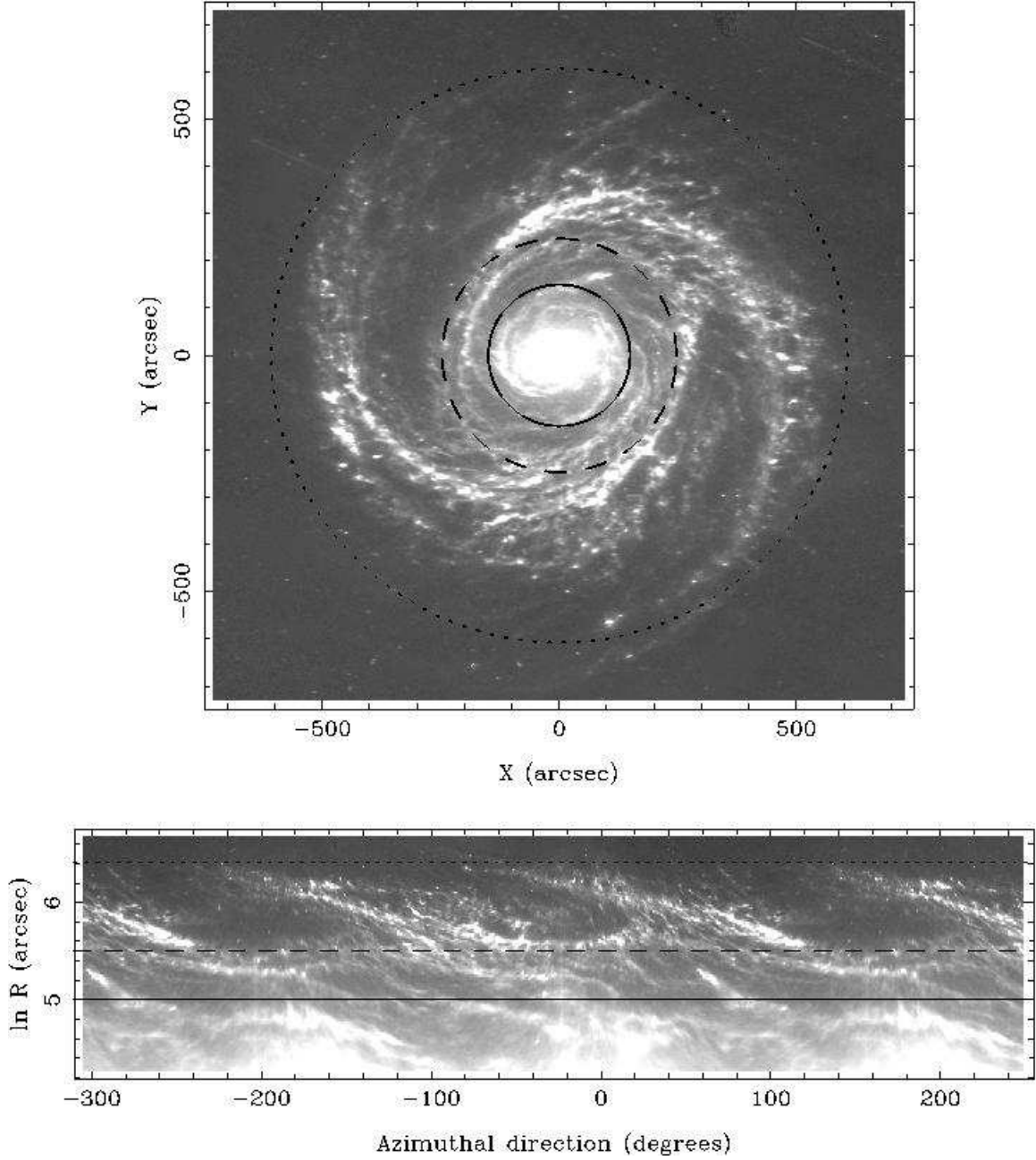


Fig. 1.— M81 deprojected image in (x, y) and in $(\ln R, \theta)$. The circles in the upper panel and the horizontal lines in the bottom panel correspond to $R = 150, 247$ and 606 arcsec, or $\ln R = 5.0, 5.5$, and 6.4 . These radii are illustrative, and were taken from Figure 2. The first value is at a minimum in the strength of the internal $m = 2$ structure, while the second is the radial position where the main long external $m = 2$ structure begins. The large radius is where the amplitude of the $m = 2$ structure decreases to 10% of its maximum value.

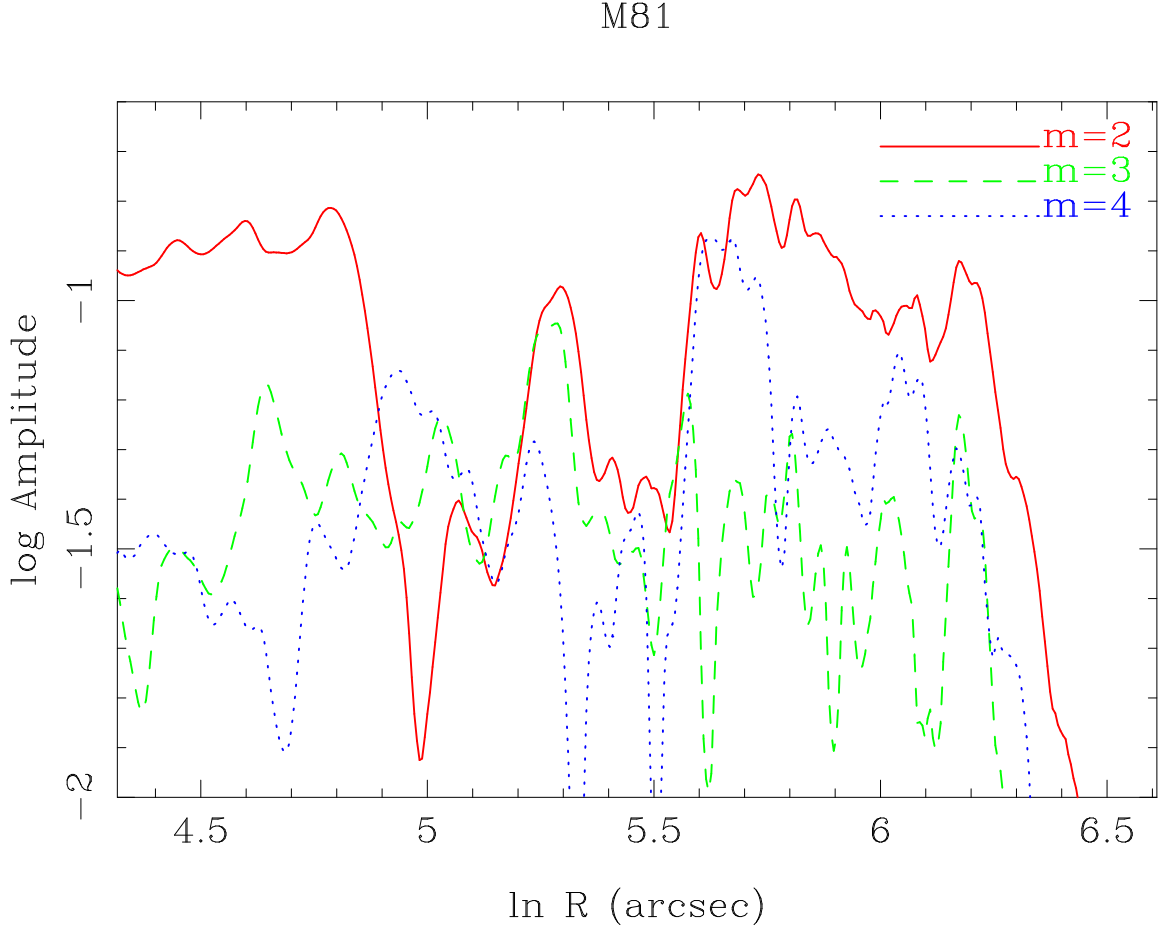


Fig. 2.— Amplitudes of the 1D Fourier transform as a function of $\ln R$ for $m = 2, 3$, and 4 . Note the valleys in the $m = 2$ curve at $\ln R = 5.0, 5.5$, and 6.4 . The corresponding radii (150, 247 and 606 arcsec) are displayed in Figure 1 (upper panel). Note that the amplitude for $m = 2$ at $\ln R = 5.0$ is only $1/3$ of the maximum amplitude. For radii larger than $\ln R = 6.4$, the amplitude of the $m = 2$ component is less than 10% of its maximum value.

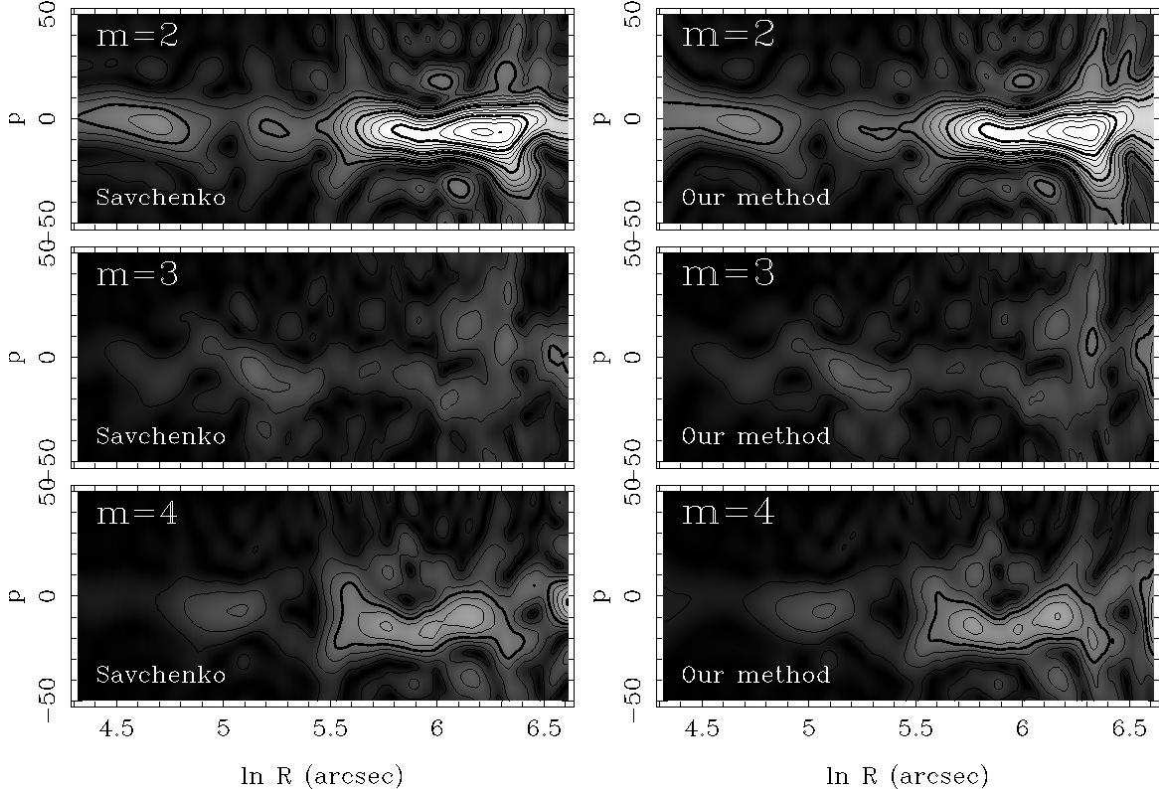


Fig. 3.— Amplitudes of the 2D Fourier transform following the Savchenko method (left) and correlation values for our method using a 2π window (right) for $m = 2, 3$, and 4 . The $\Delta \ln R$ for the calculations was $u_{max} - u_{min} = 0.35$ (see equation 2). The x axis is the same as in Figure 2. The gray scale and the contour values are the same for all of the plots. For $m = 2$, note the low amplitudes for the 2D Fourier transforms and for correlation values at $\ln R \sim 5.0, 5.5$, and 6.4 . For the Savchenko method, we plot the amplitude of the $A(m, p)$ Fourier coefficient as a function of $\ln R$ and frequency p , which is related to the pitch angle P as $\tan P = -m/p$. For our correlation method, we plot the value of the correlation for each $\ln R$ and frequency p , namely, $C_m(\ln R, \theta, p)$ (equation 4), maximized over θ .

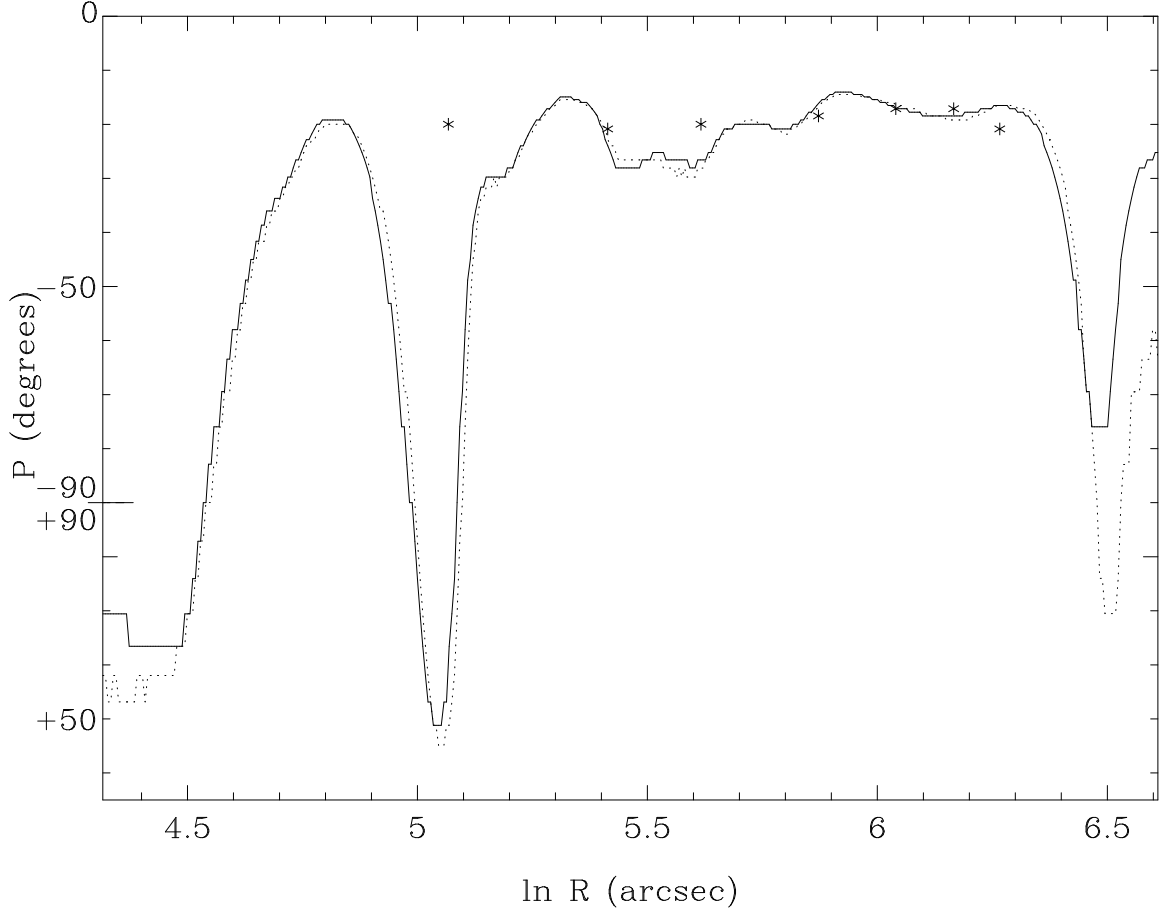


Fig. 4.— Pitch angles for the $m = 2$ component for the Savchenko method (solid line), our correlation method (dotted line), and calculated as in Davis et al. (2012) (asterisks). Note the good agreement between the three methods. The “twist” of the pitch angles around $\ln R = [5.0 - 5.1]$ occurs where $m = 2$ has a minimum in amplitude (see Figure 2). The results are not reliable for radii larger than $\ln R \sim 6.4$.

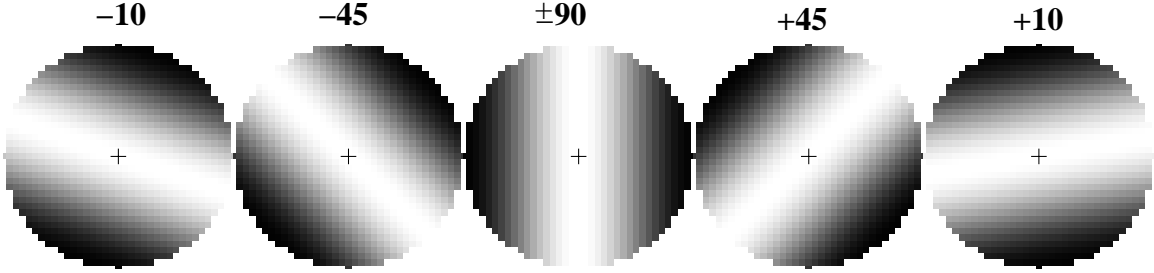


Fig. 5.— Sine filters on circular windows. Horizontal direction: azimuth; vertical direction: $\ln R$. White represents the maximum of the filter values. Each filter is normalized, i.e., the sum of all values of a given filter is always 1. Each filter is labeled with its pitch angle in degrees. The plus sign indicates the central position $(\ln R_c, \theta_c)$. Filters like these, with different diameters D_w and with pitch angles P_w varying from -1° to -90° and $+90^\circ$ to $+1^\circ$, are used to calculate the cross correlation between the galaxy image at a given $(\ln R, \theta)$ position and the filter. Higher correlations will be achieved when the structure has the same pitch angle as the filter at that $(\ln R, \theta)$ position. These correlations give a local estimate for the pitch angle. Different windows diameters D_w are used to stress the difference between large and small scale structures.

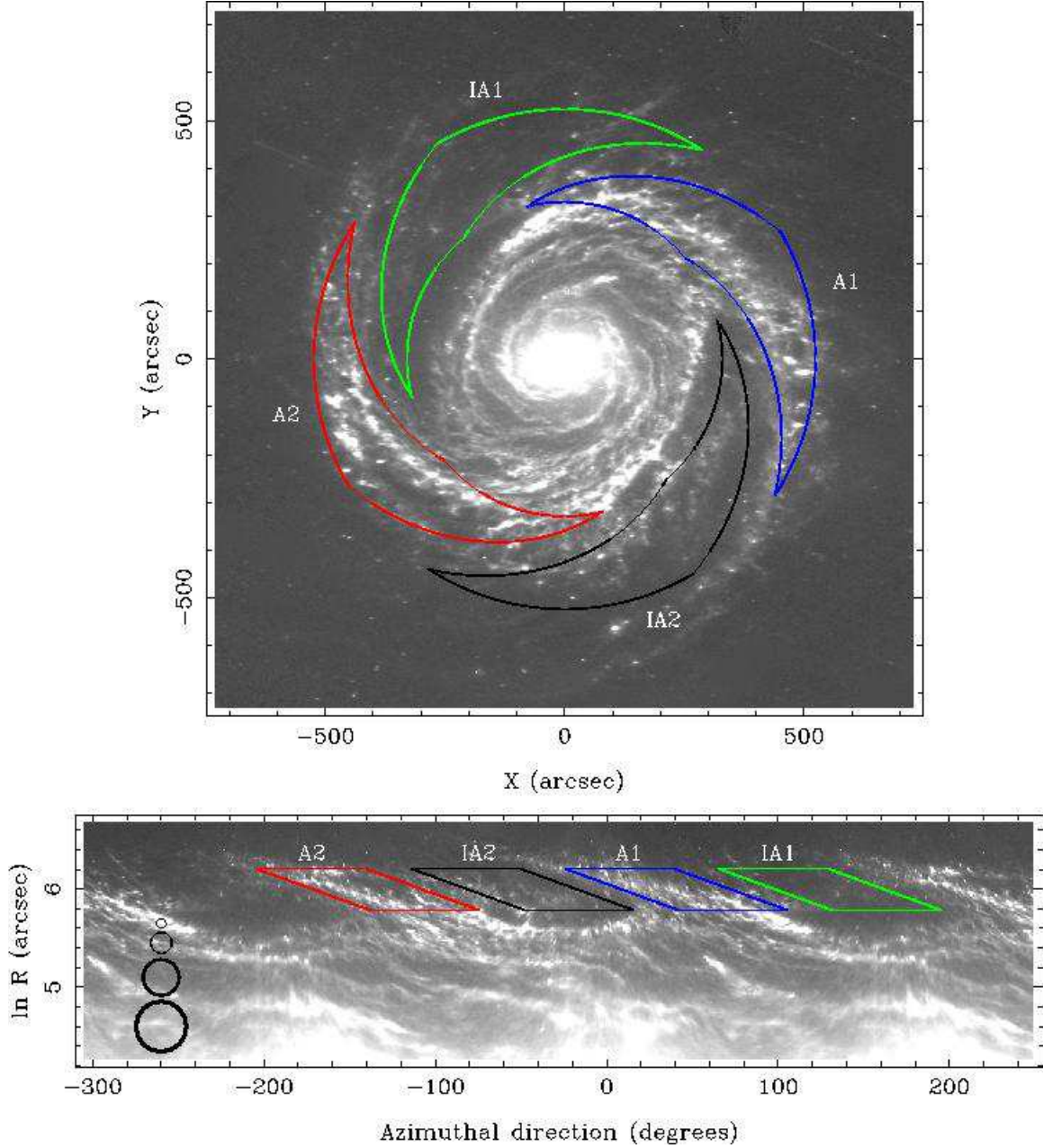


Fig. 6.— As in Figure 1, M81 in (x, y) and $(\ln R, \theta)$ representations. Here, we delineate the regions in which we add all of the correlations for a given window diameter D_w and for each pitch angle P_w . The minimum and maximum radii are 330 and 525 arcsec, corresponding to $\ln R = 5.8$ and 6.26. The arm regions (blue and red) and interarms (green and black) are marked. The circles drawn in the bottom panel represent the four different window diameters D_w we have used in this study; from top to bottom, $D_w = 0.1, 0.2, 0.35$ and 0.51 in units of $\ln R$.

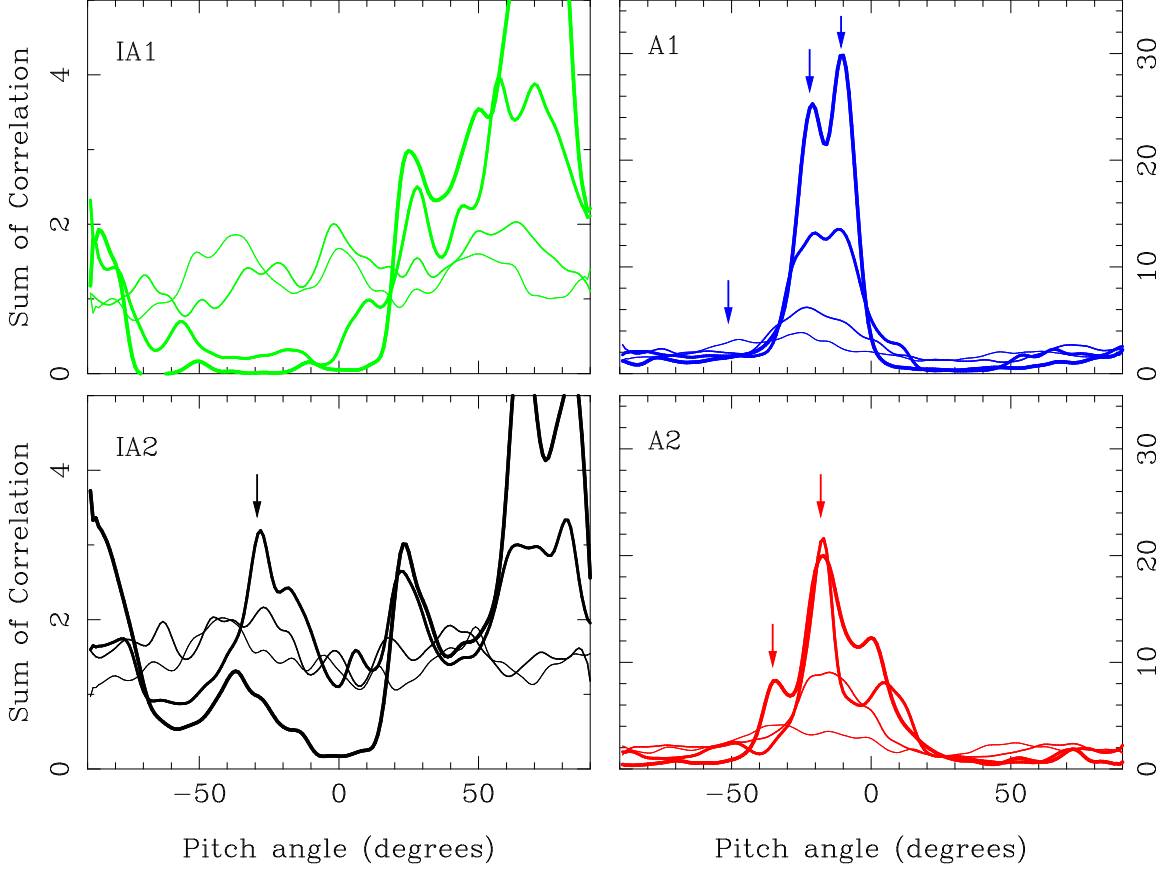


Fig. 7.— Results for the sum of the correlations in the analysed areas for M81. Green and black, interarm regions (left). Blue and red, arm regions (right). Note the different scales in the left and right panels. The thinnest line is for $D_w = 0.1$, and the thickest one is for $D_w = 0.51$. Some peaks are marked with arrows in the panels. For the interarm regions at small scales, the correlations are about the same for all pitch angles; in the black region, one intermediate scale shows a pronounced peak at $P \sim -30^\circ$. For larger scales, the correlations show contamination from the arms (notice the high correlation for pitch angles $P \geq +60^\circ$). For the arm regions at large scales, the blue area shows two peaks of pitch angles around $P = -10^\circ$ and $P = -22^\circ$; the red area has a strong peak at $P = -17^\circ$ and a secondary peak at $P \sim -38^\circ$. For smaller scales, both arm regions (blue and red) show broad peaks for $P \leq -20^\circ, -25^\circ$.

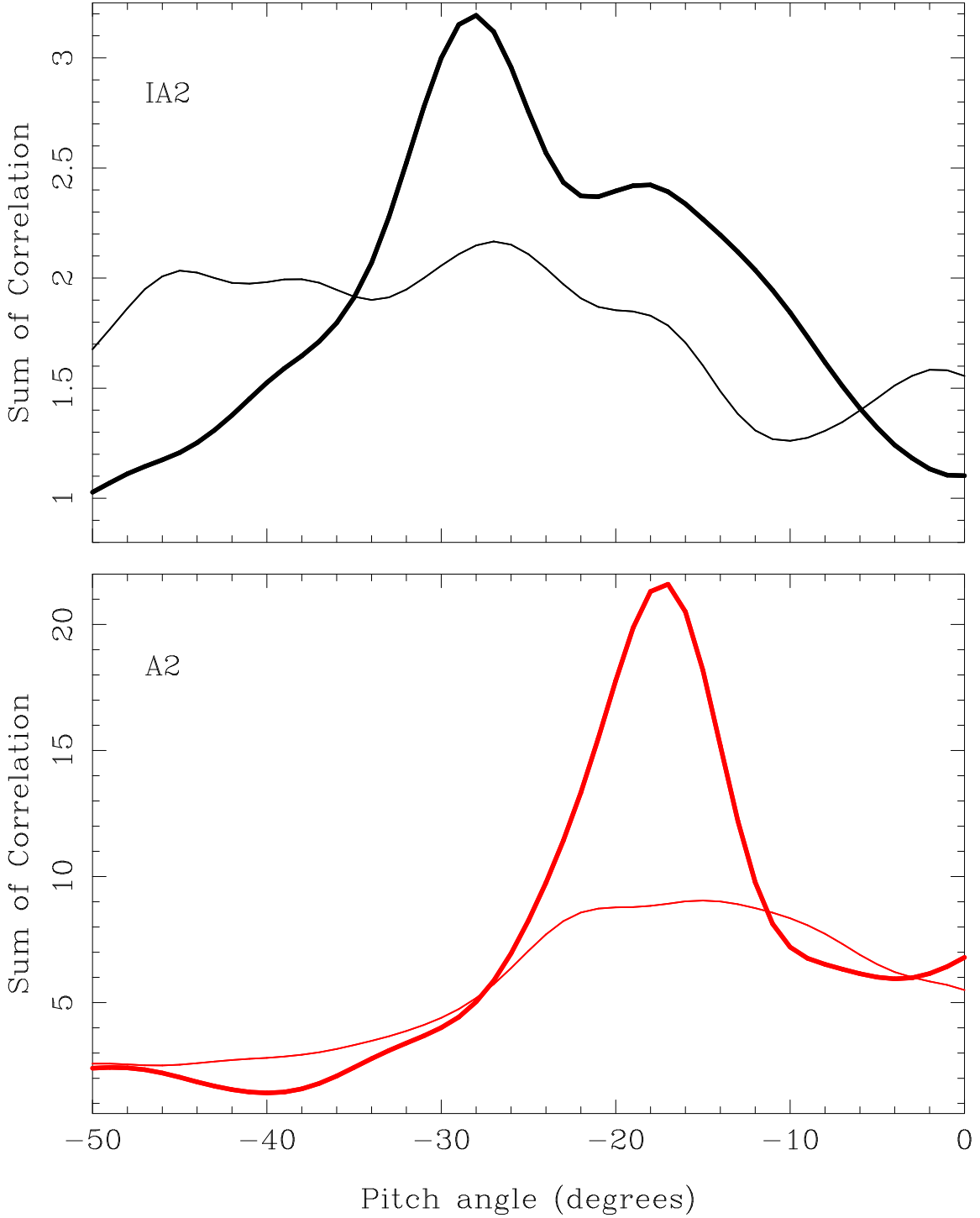


Fig. 8.— Zoom in on the sum of correlations for the black (interarm) and red (arm) regions in M81. Here we plot only the intermediary scales (thin line, $D_w = 0.2$, thick one, $D_w = 0.35$). The arm region distribution of pitch angles peaks at $P = -17^\circ$. For the interarm region, the sum of the correlations points to more open structures, with a broader distribution in pitch angles and a peak around $P = -28^\circ$.

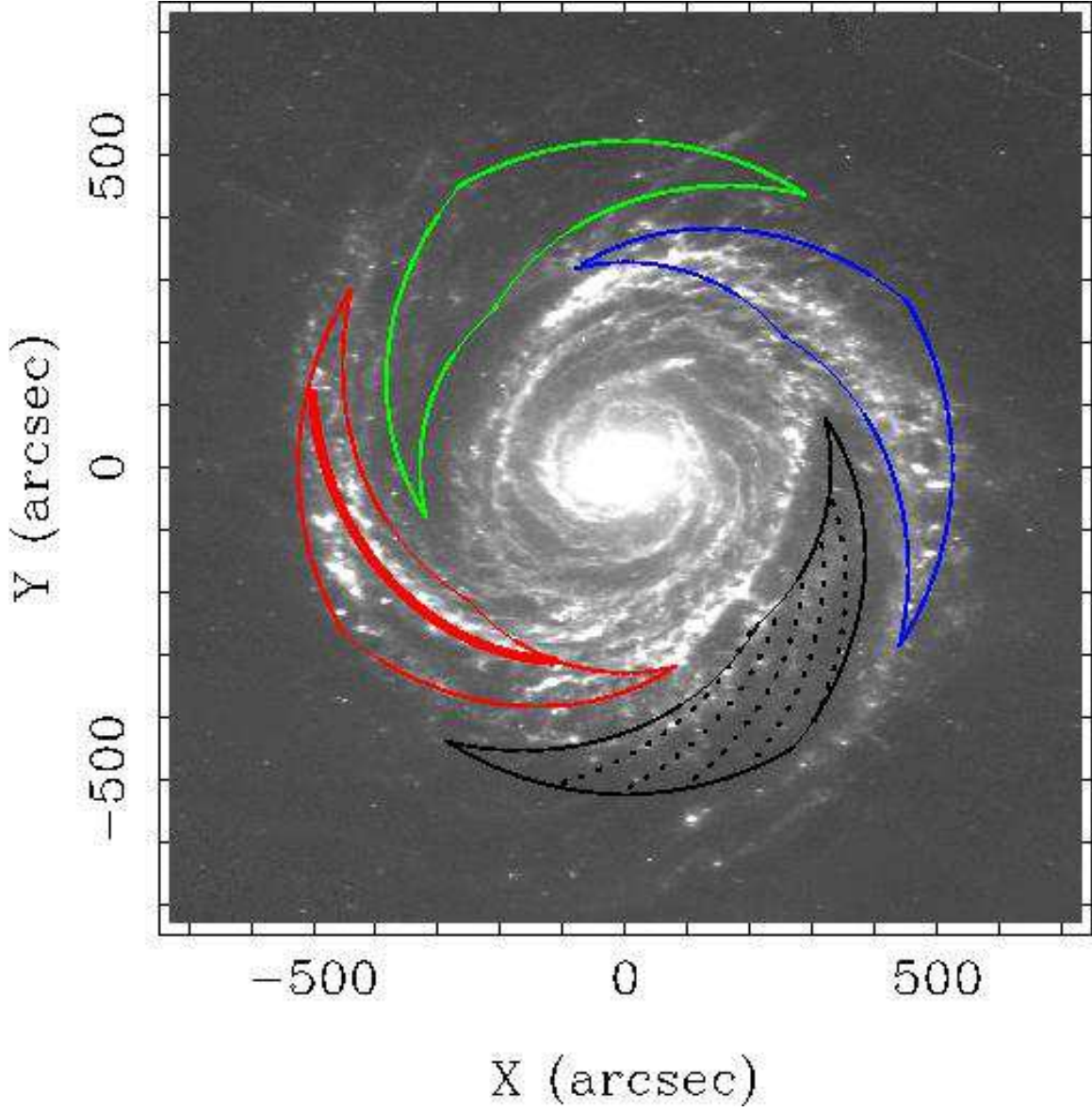


Fig. 9.— Spiral arm tracings made from the results of Figure 8 for M81. The thick solid red line represents the main spiral arm with its measured pitch angle of $P = -17^\circ$. The dotted black lines represent a pitch angle of $P = -28^\circ$. Note that these open interarm structures measured here by the correlation technique match well to the distribution of light.

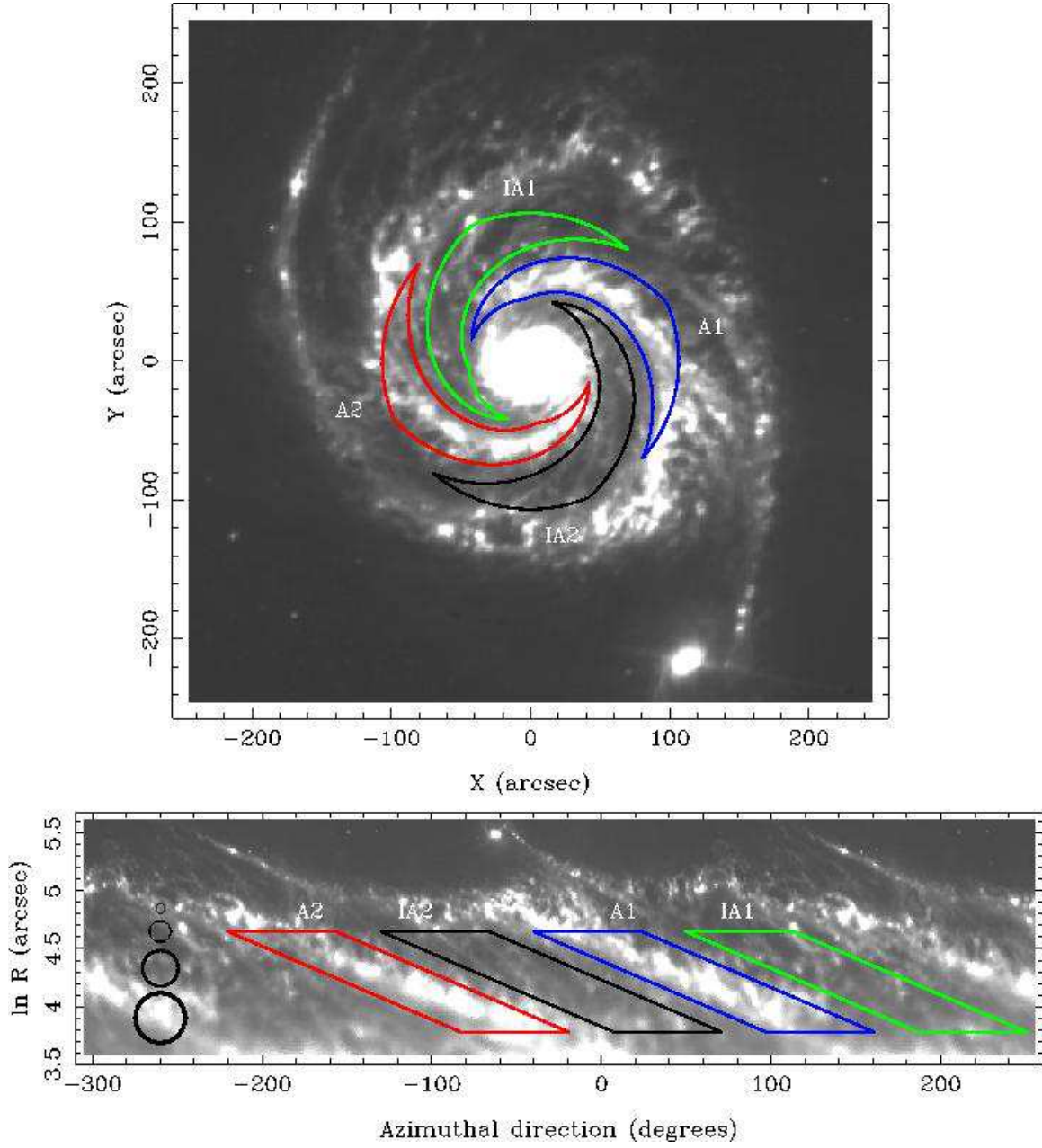


Fig. 10.— As in Figure 6, but now for M51. Here, the minimum and maximum radii are 44 and 106 arcsec, corresponding to $\ln R = 3.78$ and 4.66.

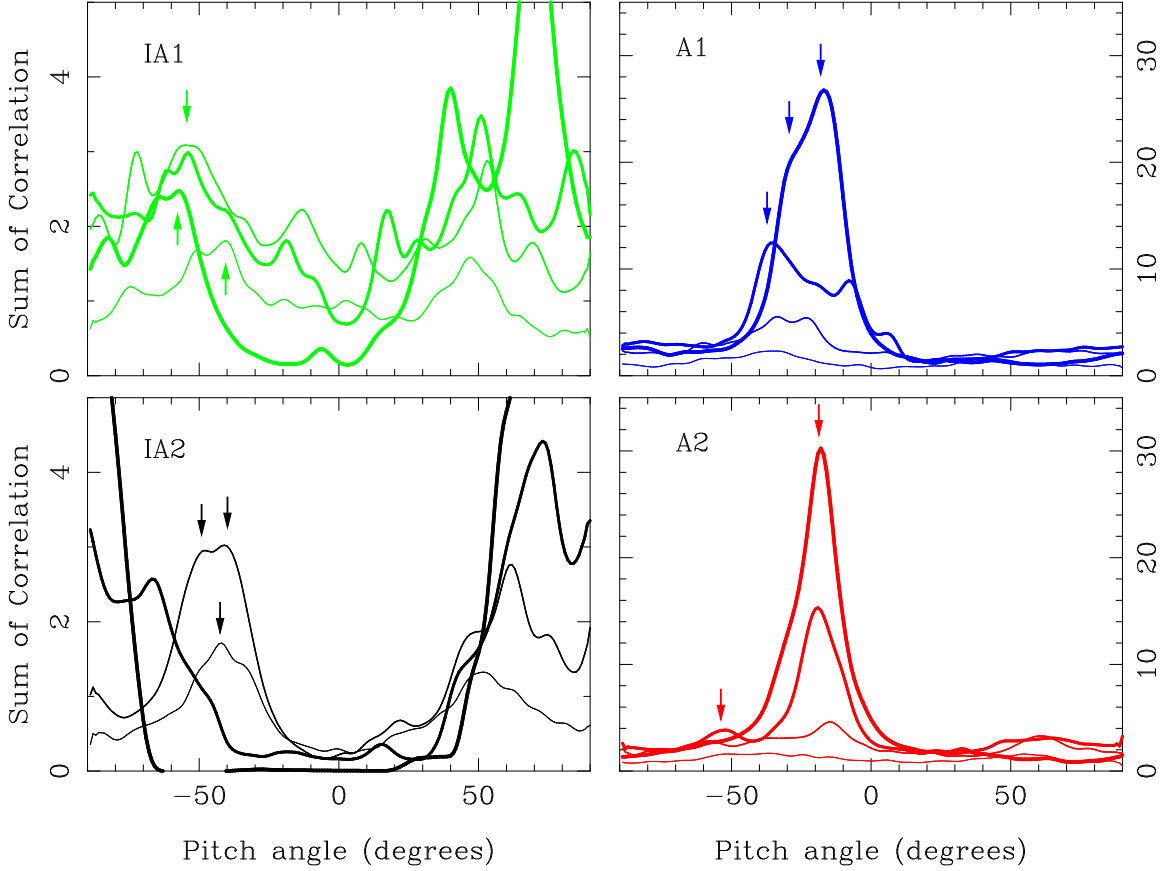


Fig. 11.— As in Figure 7, but now for M51. Green and black are interarm regions (left); blue and red are arm regions (right). Note the different scales between left and right panels. The thinnest line is for $D_w = 0.1$, while the thickest one is for $D_w = 0.51$. Some peaks are marked with arrows in the panels. The distributions of pitch angles are similar to those in M81. Here, both interarm regions (green and black) have peaks for the pitch angles at $P \leq -40^\circ$ covering a wide range of scales. The results for the arm regions (blue and red) at large scales represent the main spiral arms, with $P \sim -19^\circ$. The blue region presents an asymmetric main peak in the pitch angle distribution. For smaller scales, both arm regions have broad distributions of pitch angles, with larger values compared to that of the main spiral arms.

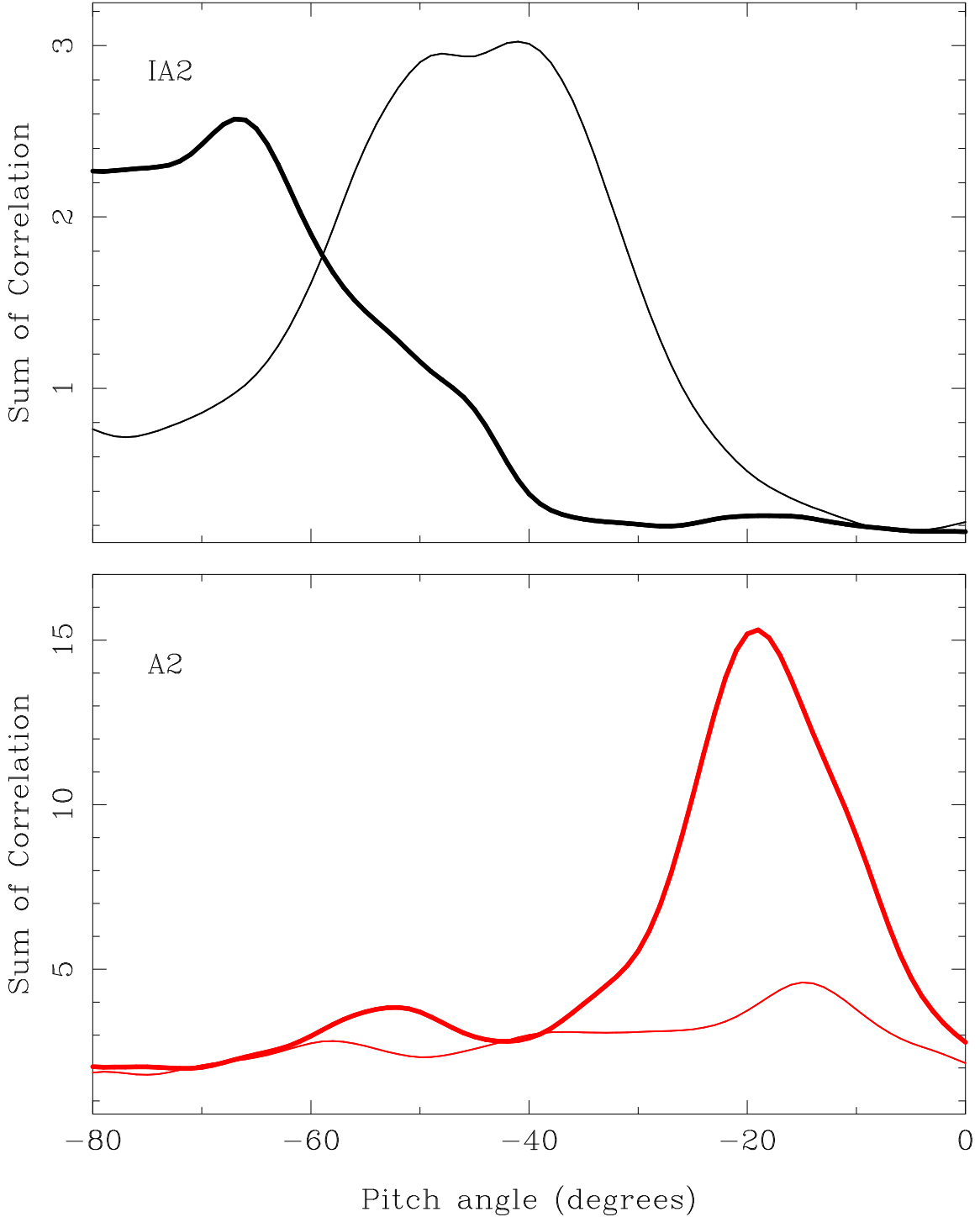


Fig. 12.— Zoom in on the sum of correlations for the black (interarm) and red (arm) regions in M51. Here we plot only the intermediary scales (thin line, $D_w = 0.2$; thick line, $D_w = 0.35$). The arm peaks at a pitch angle around $P = -19^\circ$, and presents a bump at $P \sim 52^\circ$. For the interarm region, the sum of the correlations point to more open structures, with a broader distribution in pitch angles and a peak around $P = -65^\circ$. At the small scales plotted here, the interarm region shows a broad distribution with a plateau from $P = -50^\circ$ to $P = -40^\circ$.